On the discrimination between nucleation and propagation in nanomagnetic logic devices

Cite as: AIP Advances **8**, 056003 (2018); https://doi.org/10.1063/1.5006935
Submitted: 28 September 2017 . Accepted: 09 October 2017 . Published Online: 05 December 2017

Grazvydas Ziemys, Gyorgy Csaba, and Markus Becherer

On the discrimination between nucleation and propagation in nanomagnetic logic devices

Grazvydas Ziemys,[1,a] Gyorgy Csaba,[2] and Markus Becherer[3]
[1]*Chair of Circuit Design, Technical University of Munich (TUM), Germany*
[2]*Faculty of Information Technology and Bionics, Pázmány Péter Catholic University Budapest, Hungary*
[3]*Chair of Nanoelectronics, Technical University of Munich (TUM), Germany*

(Presented 9 November 2017; received 28 September 2017; accepted 9 October 2017; published online 5 December 2017)

In this paper we present the extensive nucleation and propagation characterization of fabricated nanomagnets by applying ns-range magnetic field pulses. For that, an artificial nucleation center (ANC) is created by focused ion beam irradiation (FIB) of a 50 x 50 nm area at the side of a Co/Pt island as typically used in Nanomagnetic Logic with perpendicular anisotropy (pNML). Laser-Kerr Microscope is applied for statistical evaluation of the switching probability of the whole magnet, while the wide-field-Kerr microscopy is employed to discriminate between the nucleation process (which takes place at the irradiated ANC area) and the domain wall propagation process along the magnet. We show that the nanomagnet can be treated as a single Stoner-Wolfhart particle above 100 ns field-pulse width, as the whole magnetization is switched during the field-pulse. By contrary, for field-pulse width below 100 ns, the domain wall (DW) motion is the limiting process hindering full magnetization reversal on that time-scale. However, the nucleation still follows the Arrhenius law. The results allow precise understanding of the reversal process and highlight the need for faster DW speed in pNML materials. https://doi.org/10.1063/1.5006935

I. INTRODUCTION

Nanomagnetic Logic (NML) is a strong candidate for the Beyond CMOS scaling era and for that is listed in the latest International Technology Roadmap for Semiconductors 2015 (ITRS) in the "Beyond CMOS" technology chapter.[1] NML is compatible with the existing CMOS technology and can be integrated on the same CMOS die in the back-end-of-the line process (BEOL). Such hybrid integration allows to use the advantages of both technologies. First benchmarking against CMOS shows that NML consumes at least 35 times less energy for NAND/NOR operation, compared to CMOS.[2] Moreover, stacking several functional layers of NML on top of each other allows ultra high integration densities. This is achieved by employing monolithic 3D integration, as experimentally proven by Eichwald et al.[3,4] Furthermore, NML comprises memory and logic functionality in a single technology.[5] In NML a current computational state is retained even with no energy supply. NML has several advantages over the CMOS and can be most beneficial for implementing co-processor, pattern matching hardware, or parallel, deeply pipelined and high throughput data processing in big data applications.[6] It also allows to explore new kind of data processing architectures and paradigms. NML is one of the most competitive and experimentally proven candidates for the Beyond-CMOS devices research field.

In this work we concentrate on NML with perpendicular magnetic anisotropy (PMA), which arises from ultra-thin Co/Pt multilayer films. NML based on PMA is called pNML. This technology is

[a]g.ziemys@tum.de

based on bistable nanomagnets where the logical states ('1' and '0') are encoded in the magnetization vector. Due to crystallinity and interfaces of Co/Pt thin films, the magnetization vector has only two stable states (up and down) parallel to the surface normal of the magnet. Logic operations are carried out by magnetic field-coupled nanomagnets. The most basic pNML element is an inverter, which consists of two magnets placed close to each other. Due to the fact that all systems try to minimize their energy, the magnetization vectors of these two magnets align anti-parallel to each other. Directionality of the signal is ensured by the generation of a weak spot on one side of a nanomagnet.[7] This ensures that e.g. the magnet on the right is only sensitive to the one on the left side. The weak spot is called artificial nucleation center (ANC) and is generated by irradiation of an area of typically 50 x 50 nm with a focused ion beam (FIB), which locally reduces the magnetic anisotropy by intermixing the Co/Pt layers and thus sensitizing the nanomagnet to the magnetic stray fields of the neighboring nanomagnets on one side.[8,9] The key element of the nanomagnetic logic is the majority gate.[10] Fixing one of three inputs of a majority gate leads to a NAND/NOR gate depending on the state of the fixed input. This allows to build an arbitrary Boolean logic function. To propagate the information through such gates, an external alternating magnetic field is needed. The amplitude of this field is set in such a way, that the magnets can only switch if the superposition of the stray field of the neighboring magnet and the external field is constructive. Such alternating field acts as a clock signal and it also provides the energy for the system. The clocking field is generated globally by the on-chip metal conductor. An on-chip meander-like current conductor structure, embedded between a high μ_r material, such as Permalloy, is used to minimize the electrical current, needed to generate the clocking field.[11]

Despite the benefits of pNML, it still needs to be investigated and optimized for higher clocking rates. In order to achieve that, it is crucial to investigate and characterize the magnetic switching of the nanomagnets with a realistic geometry, as used for pNML by applying ns-range magnetic pulses. Until now such measurements were done integrally by evaluating the magnetization state of the whole nanomagnet with a laser Kerr-effect microscope.[12,13] In this paper, additionally to laser Kerr-effect microscope, we employ a wide-field Kerr-effect microscope. This allows spatial magnetization evaluation and, therefore, precise differentiation between nucleation and propagation in on-chip applied magnetic field pulses. This enables to refine pNML compact models and, therefore, build even more realistic circuits clocked in the targeted GHz-range. The hardware calibrated models can be subsequently applied to explore new computing architectures.

II. MAGNETIC SWITCHING

For compact modelling a typical pNML magnet can be subdivided into three parts: Artificial nucleation center, magnetic nanowire, and magnetic output field generator.[14] Magnetization reversal of a pNML magnet with typical geometry as exemplified by Fig. 1a) includes two steps. First, a domain wall (DW) is generated at the area of local reduced anisotropy (ANC). Afterwards, DW is propagated through the entire magnet. The latter step can be considered as DW movement in a magnetic nanowire. The *output field generator* is a part of a magnet with a relatively large area to generate the highest possible stray field, which then superposes with an external magnetic clocking

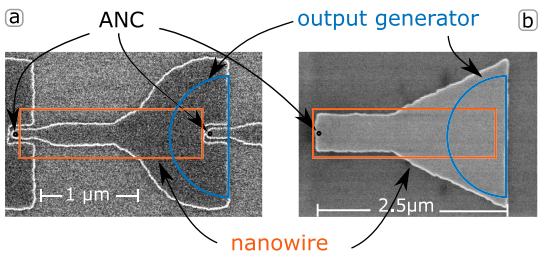

FIG. 1. a) SEM image of a typical pNML magnets geometry fabricated from a Co/Pt multilayer film. Shown magnet is a part of an inverter chain circuit and, therefore, placed between two neighboring magnets. b) SEM image of the investigated magnet. Both images show the three main parts: ANC, nanowire, and an output generator, as used for modeling the pNML.

field and acts on the ANC of the neighboring magnet. High stray fields result in higher coupling of the magnets and, therefore, more reliable pNML circuits.

It is commonly accepted that the field needed to switch the magnet (H_c) follows an Arrhenius law, which describes the probability of thermally assisted processes. It can be expressed in the equations below:

$$P_{sw}(t_p, H_{0,ANC}) = 1 - \exp(-t_p/\tau(H_{eff})) \tag{1}$$

and

$$\tau(H_{eff}) = f_0^{-1} \exp\left(\frac{E_{0,ANC}(1 - \frac{H_{eff}}{H_{0,ANC}})^2}{k_b T}\right) \tag{2}$$

where t_p is the time interval during which the effective magnetic field acts on ANC, f_0 = 2GHz the reversal attempt frequency, k_b the Boltzmann constant, and T the temperature in Kelvin. The parameters $E_{0,\,ANC}$ and $H_{0,ANC}$ define the switching characteristics of a nanomagnet. $E_{0,ANC}$ describes the energy barrier of the ANC when no external field is applied, and can be noted as follows:

$$E_{0,ANC} = K_{ANC} V_{ANC} \tag{3}$$

K_{ANC} is determined by the irradiation dose. The dose of $4{\cdot}10^{13}$ ions/cm^2 through the 100 nm PMMA resist was applied during the lithography process. We assume that the irradiation reduces the anisotropy to 40% of the K_{eff}. K_{eff} was measured prior to the structuring the magnets in multilayer film ($Ta_{3nm}/Pt_{3nm}/4x[Co_{0.8nm}/Pt_{1.5nm}]/Pt_4$) and yields $K_{eff} = 2.7 \cdot 10^5$ J/m^3. $H_{0,ANC}$ is the field required to change the magnetization direction of an ANC at zero temperature,

$$H_{0,ANC} = \frac{2K_{ANC}}{\mu_0 M_s}; M_s = M_{s,co}\frac{t_{co}}{t_{stack}} \tag{4}$$

where μ_0 is the vacuum permeability and M_s the saturation magnetization, and is calculated based on the composition of the film stack as follows: where the $M_{s,co} = 1.4 \cdot 10^6$A/m is the literature value of cobalt saturation magnetization, t_{co} is the total thickness of cobalt in the complete ML stack t_{stack} excluding seed and capping layer. Expressing the Arrhenius equation to H_{eff} and fixing the switching probability to 50% (p_{sw} = 0.5) gives the Sharrock formula.[15]

To investigate the statistics of magnetic switching of a typical pNML magnet, a laser Kerr-effect microscope measurements were performed. For that the magnet shown in Fig. 1 (b) was investigated applying magnetic pulses with different lengths and amplitudes. Switching field distribution plots and Arrhenius curves for pulse lengths from 700 ms to 20 ns can be found in Ref. 14. This work concentrates on the Sharrock plot, which is obtained by evaluating the Arrhenius plot as described above. In particular reasons for the deviation of the experimental data from Arrhenius law are investigated. It is observed that for longer than 100 ns pulses the experiment can be well fitted to the Arrhenius law with one parameter set, however, this is not possible for the short pulses.

III. EXPERIMENT SETUP AND RESULTS

Evaluation of magnetization was carried out using the Laser Kerr-effect measurements after applying the following steps: the magnet was saturated by applying high magnetic field in both positive and negative direction perpendicular to the sample surface. Afterwards, the magnetic pulse of interest was applied, followed by the propagation pulse. A pulse amplitude for the propagation is carefully estimated prior to the beginning of the experiment at highest field, which is still not able to switch the magnet. This sequence is plotted in the Fig. 2.

Fig. 3 presents the Sharrock plot of the investigated magnet. The orange dots represent 50% switching probability for different pulse lengths and amplitudes, obtained by measuring with laser the Kerr-effect microscope. It can be seen that the Arrhenius model can be fitted to the experimental data very well until pulse lengths of 100 ns. For shorter pulses a steep increase of the field amplitude is observed. We demonstrated that this behavior could be modelled by increasing damping constant α

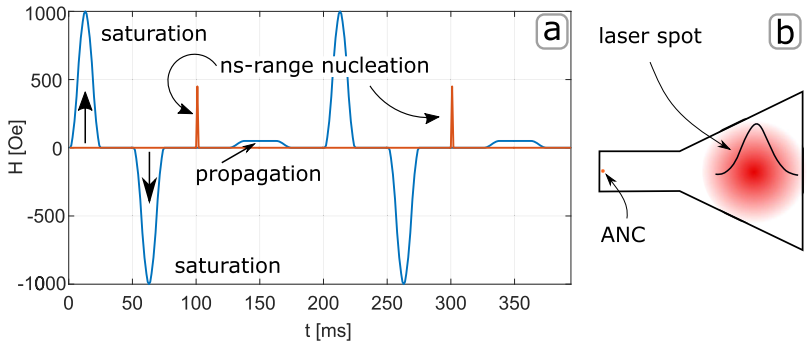

FIG. 2. a) Sequence of measurement steps: saturation, nucleation by ns-rang pulse, propagation field. b) Schematic visualization of focused laser spot position during the measurements.

to the value of 50, as presented by the yellow line in Fig. 3.[13] Such high damping values are somewhat not expected and lack physical explanation. However, for compact modeling of a magnet as a "black box" it appeared sufficient.

To investigate the behavior of the magnet more precisely, we employed wide-field MOKE microscope (WMOKE). WMOKE allows spatially resolved measurements and, therefore, evaluation of magnetization across the whole magnet at the same time. Measurements were performed as follows: first, the magnet was saturated and then, the ns-range pulse was applied, after that, the image was taken. The images after 12.5 ns long 204 Oe and 25 ns long 330 Oe pulses are presented in Fig. 4 a) and b) respectively. To extract magnetic information from the taken images, the topography needs to be subtracted from the original images. This is done in two ways to further enhance the contrast of magnetic information. Images in Fig. 4 at the top and bottom represent the same information, but are obtained in two different ways. From the top images, the reference image, which includes just the topography, is subtracted. The bottom ones are differential images, obtained by subtracting the images before and after the applications of the nucleation pulse. The reference image is generated by adding the magnetic positive and negative saturated images and then dividing the resulting image by two. Such an image contains only topography of the surface, but no magnetic information. In the bottom images only the magnetization difference, evoked by the nucleation pulse, should be visible, in contrast where in the images at the top - the magnetization of the whole magnet is visible. The bright spots represent up-, while the dark part - down-magnetization.

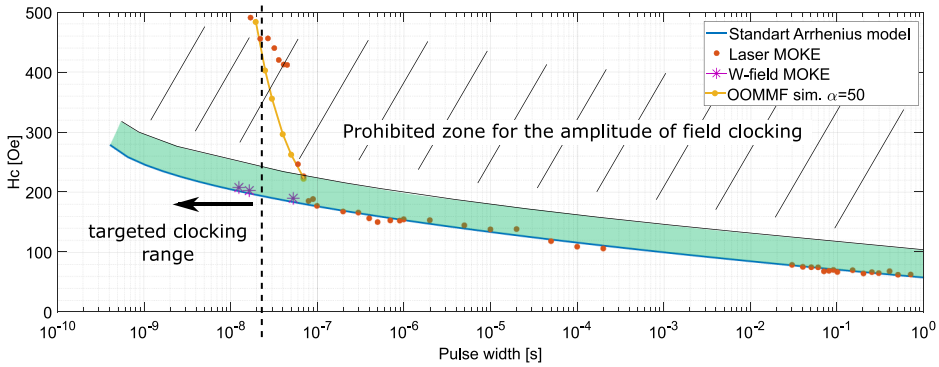

FIG. 3. Sharrock plot of the investigated magnet, winch gives the 50% magnetic switching probability versus time. Orange dots represent the laser MOKE, while violet markers - the wide field MOKE measurements. Blue solid line shows the Arrhenius equation fitted to the laser MOKE data. The yellow line represents the OOMMF simulations for high damping constant, which allows to model the switching of the whole magnet. Green area marks the safe pNML clocking zone for investigated magnet, where nucleation is ensured to happen at the ANC.

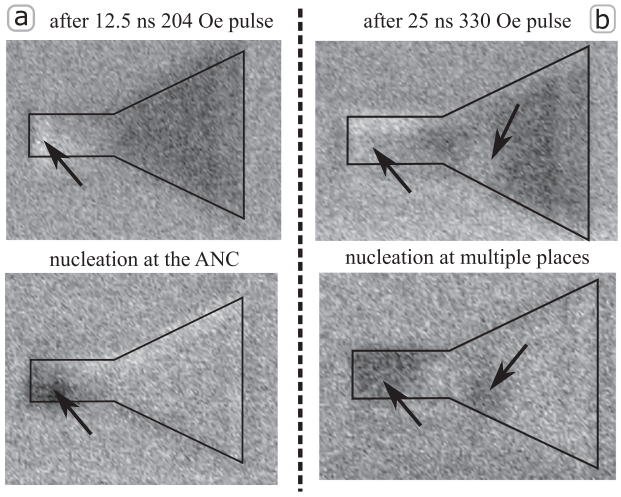

FIG. 4. Wide-field MOKE images of the investigated magnet after 12.5 ns 204 Oe pulse (a) and after 25 ns 330 Oe pulse (b). Top and bottom images represent the same information. To enhance the ability to distinguish up- and down-magnetized parts of the magnet, they are processed differently. Top: topography subtracted images, bottom: differential images obtained by subtracting the image after the pulse form the image before. Arrows points to the DWs generated by the nucleation pulse. For the pulse with 204 Oe amplitude, the new DW is generated only at the ANC (a), for 330 Oe pulse several nucleation sites are observed (b).

IV. DISCUSSION

Wide-field microscope measurements reveal two important processes. Firstly, at high amplitudes (H>226.7 Oe) the nucleation of the new domain walls occurs not only at the ANC, but also at more spots, as can be seen in the Fig. 4 (b). Secondly, the length of the propagation pulse should be at the same order of magnitude as the nucleation pulse, otherwise it does not propagate the generated domain wall, or it also leads to the nucleation of a new DWs. E.g. the nucleation of a DW with 50% probability by the pulse lengths of 16.5 ns requires a pulse amplitude of 202.8 Oe. To propagate the generated DW, a pulse with amplitude of at least 162 Oe is needed if the pulse width is kept the same. The gap between the nucleation and propagation becomes even smaller when using longer pulses. The green area in Fig 4 marks safe clocking fields amplitudes window, where the nucleation is ensured to occur at the ANC.

The violet star markers in Fig. 3 show the 50% nucleation probability, observed with the wide-field microscope. This proves that the nucleation of a new DW follows the Arrhenius law also for the short pulses (t_p=12.5 ns). To switch the whole magnet i.e. to propagate the nucleated DW, a pulse train of at least five pulses with the same parameters as the nucleation pulse is needed. This allows to estimate the DW velocity of 50 m/s for the pulses with the amplitude of 204 Oe. The deviation of the orange dots (laser MOKE measurements) from the Arrhenius law arises due to the integral measurements of the whole magnet, as partial magnetization reversal is not registered by this method of measurements. The applied propagation pulse of 50 Oe amplitude and 700 ms width, as used in laser moke setup, is not able to propagate the nucleated DW through the magnet.

To investigate the influence of the geometry of a magnet on DW propagation, the whole magnet was simulated in OOMMF[16] for different external field pulses. The simulation results show that the pinning barrier at the point where the magnet gets wider, (for anisotropy $K_{eff} = 3.2 \cdot 10^4$ J/m^3), is less than 10 Oe, even when simulated at 0K temperature. K_{eff} is estimated to be 90% of measured film anisotropy due to FIB lithography, which slightly reduces the anisotropy of structures at the time of patterning. Non-existence of the pining barrier was also observed in the wide-field MOKE measurements. Simulations data also shows that nucleated DW, even by the shortest 12 ns pulse, do not collapse right after the nucleation. A nucleation happens and a new DW is generated in range of 1-3 ns at least for the assumed damping constant of $\alpha = 0.5$. This value is considered to be realistic for our multilayer films. We asked several cooperation partners to measure the damping constant,

though no ferromagnetic resonance (FMR) peaks were observable on those films. This indicates a rather large damping constant ($\alpha > 0.3$), which is in agreement with our simulations.

V. CONCLUSION

Spatially resolved measurements with the wide-field MOKE microscope prove that the nucleation of the typical pNML magnet follows Arrhenius law, and reveals that the gap of the magnetic field amplitude between nucleation and propagation pulse decreased with longer pulses. This is especially important for refining the pNML compact models and designing pNML systems. To speed up the pNML, DMI enhanced multilayer stacks are envisioned, e.g. in Pt/Co/Gd film DW wall propagation velocity of 650 m/s was reported.[17]

[1] "The International Technology Roadmap for Semiconductors (ITRS 2.0): BEYOND CMOS," (2015).
[2] M. Becherer, J. Kiermaier, S. Breitkreutz, I. Eichwald, G. Žiemys, G. Csaba, and D. Schmitt-Landsiedel, Solid-State Electronics **102**, 46 (2014).
[3] I. Eichwald, S. Breitkreutz, J. Kiermaier, G. Csaba, D. Schmitt-Landsiedel, and M. Becherer, Journal of Applied Physics **115**, 17E510 (2014).
[4] I. Eichwald, S. Breitkreutz, G. Ziemys, G. Csaba, W. Porod, and M. Becherer, Nanotechnology **25**, 335202 (2014).
[5] R. P. Cowburn and M. E. Welland, Science **287**, 1466 (2000).
[6] J. Hutchby, "The nanoelectronics roadmap," in *Emerging Nanoelectronic Devices* (John Wiley & Sons Ltd, 2014) pp. 1–14.
[7] J. Kiermaier, S. Breitkreutz, I. Eichwald, M. Engelstädter, X. Ju, G. Csaba, D. Schmitt-Landsiedel, and M. Becherer, Journal of Applied Physics **113**, 17B902 (2013).
[8] S. Breitkreutz, A. Fischer, S. Kaffah, S. Weigl, I. Eichwald, G. Ziemys, D. Schmitt-Landsiedel, and M. Becherer, Journal of Applied Physics **117**, 17B503 (2015).
[9] J. H. Franken, M. Hoeijmakers, R. Lavrijsen, and H. J. M. Swagten, Journal of Physics: Condensed Matter **24**, 024216 (2012).
[10] S. Breitkreutz, J. Kiermaier, I. Eichwald, X. Ju, G. Csaba, D. Schmitt-Landsiedel, and M. Becherer, IEEE Transactions on Magnetics **48**, 4336 (2012).
[11] M. Becherer, S. Breitkreutz, I. Eichwald, G. Ziemys, J. Kiermaier, G. Csaba, and D. Schmitt-Landsiedel, in EUROSOI-ULIS 2015: 2015 Joint International EUROSOI Workshop and International Conference on Ultimate Integration on Silicon (2015) pp. 121–124.
[12] G. Žiemys, C. Trummer, S. B.-v. Gamm, I. Eichwald, D. Schmitt-Landsiedel, and M. Becherer, AIP Advances **6**, 056404 (2016), https://doi.org/10.1063/1.4944336.
[13] G. Žiemys, S. B. v. Gamm, G. Csaba, D. Schmitt-Landsiedel, and M. Becherer, AIP Advances **7**, 056625 (2017).
[14] G. Žiemys, A. Giebfried, M. Becherer, I. Eichwald, D. Schmitt-Landsiedel, and S. B. V. Gamm, Solid-State Electronics **125**, 247 (2016), extended papers selected from {ESSDERC} 2015.
[15] M. P. Sharrock, Journal of Applied Physics **76**, 6413 (1994).
[16] M. J. Donahue, D. G. Porter, and National Institute of Standards and Technology (U.S.), OOMMF user's guide (1999).
[17] T. H. Pham, J. Vogel, J. Sampaio, M. Vaňatka, J.-C. Rojas-Sánchez, M. Bonfim, D. S. Chaves, F. Choueikani, P. Ohresser, E. Otero, A. Thiaville, and S. Pizzini, EPL (Europhysics Letters) **113**, 67001 (2016).